ACS APPLIED MATERIALS & INTERFACES

www.acsami.org

Research Article

Nanoscale Heterogeneities of Non-Noble Iron-Based Metallic Glasses toward Efficient Water Oxidation at Industrial-Level Current Densities

Zhe Jia, Yilu Zhao, Qing Wang, Fucong Lyu, Xiaobao Tian, Shun-Xing Liang, Lai-Chang Zhang, Junhua Luan, Qianqian Wang, Ligang Sun,* Tao Yang,* and Baolong Shen*

Cite This: *ACS Appl. Mater. Interfaces* 2022, 14, 10288−10297

Read Online

ACCESS | Metrics & More | Article Recommendations | Supporting Information

ABSTRACT: Scaling up the production of cost-effective electrocatalysts for efficient water splitting at the industrial level is critically important to achieve carbon neutrality in our society. While noble-metal-based materials represent a high-performance benchmark with superb activities for hydrogen and oxygen evolution reactions, their high cost, poor scalability, and scarcity are major impediments to achieve widespread commercialization. Herein, a flexible freestanding Fe-based metallic glass (MG) with an atomic composition of $Fe_{50}Ni_{30}P_{13}C_7$ was prepared by a large-scale metallurgical technique that can be employed directly as a bifunctional electrode for water splitting. The surface hydroxylation process created unique structural and chemical heterogeneities in the presence of amorphous FeOOH and Ni_2P as well as nanocrystalline Ni_2P that offered various active sites to optimize each rate-determining step for water oxidation. The achieved overpotentials for the oxygen evolution reaction were 327 and 382 mV at high current densities of 100 and 500 mA cm^{-2} in alkaline media, respectively, and a cell voltage of 1.59 V was obtained when using the MG as both the anode and the cathode for overall water splitting at a current density of 10 mA cm^{-2}. Theoretical calculations unveiled that amorphous FeOOH makes a significant contribution to water molecule adsorption and oxygen evolution processes, while the amorphous and nanocrystalline Ni_2P stabilize the free energy of hydrogen protons (ΔG_{H^*}) in the hydrogen evolution process. This MG alloy design concept is expected to stimulate the discovery of many more high-performance catalytic materials that can be produced at an industrial scale with customized properties in the near future.

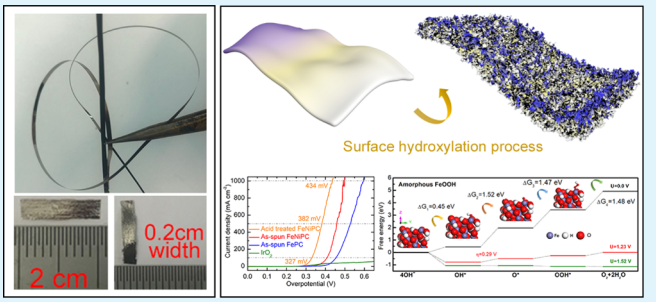

KEYWORDS: *metallic glasses, heterogeneity, chemical complexity, water oxidation, metallurgy*

INTRODUCTION

Water electro-splitting has been widely identified as a particularly promising and appealing technology for the sustainable production of hydrogen, which opens up the possibility to replace traditional fossil fuels with a carbon-neutral alternative.[1−3] Two half-reactions, including the hydrogen evolution reaction (HER) on cathodes and the oxygen evolution reaction (OER) on anodes, are involved into the overall water-splitting process.[4] Thus, exploring low-cost and environmentally friendly bifunctional electrodes for both efficient HER and OER is the currently remaining challenge. To date, great research effort has been dedicated to developing novel electrocatalysts by nanostructuring,[5] doping,[6] alloying,[7] and compositing[8] to achieve enhanced water-splitting activity. However, these state-of-the-art laboratory-scale prepared electrocatalytic materials are still hampered seriously by their limited activity and durability at large current densities, while their complicated electrode preparation processes bring into question their industrial scalability.[9] Accordingly, there is a great demand for the large-scalable manufacturing of cost-effective, free-standing, high-performance, and long-term stable electrocatalysts to substitute for currently used high-cost materials; however, achieving this goal is still extremely challenging.

To address these requirements, MGs (also referred to as amorphous alloys), with several unique characteristics of multicomponents,[10−12] structural heterogeneities,[13−15] metastable nature,[16−18] high atomic diffusion rate,[19−21] and so forth, have demonstrated great potential for the discovery and development of novel catalysts.[22] Particularly, it was found that $Pd_{40}Ni_{10}Cu_{30}P_{20}$ MGs with their intrinsic chemical hetero-

Received: November 16, 2021
Accepted: February 7, 2022
Published: February 17, 2022

https://doi.org/10.1021/acsami.1c22294
ACS Appl. Mater. Interfaces 2022, 14, 10288−10297

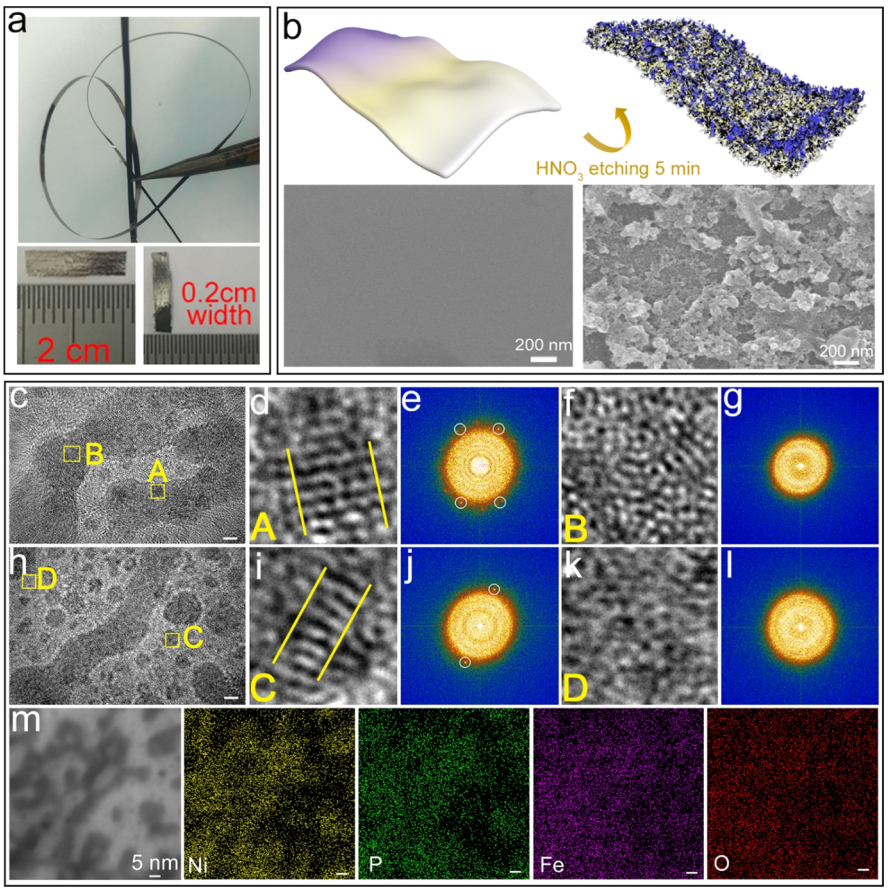

Figure 1. Conceptional design and microscopy characterization. (a) Optical photographs of the as-spun FeNiPC MG. (b) Schematic illustration and surface morphological evolution of the as-spun and acid-treated FeNiPC MG. (c,h) HRTEM images of the acid-treated FeNiPC MG showing nanoscale heterogeneities (scale bar, 2 nm). (d,f,i,k) HRTEM images of the A, B, C, and D regions from (c,h). A, C and B, D regions showing nanocrystalline and amorphous structures, respectively. (e,g,j,l) Corresponding FFT patterns of the regions in (d,f,i,k), respectively. The bright spots in (e,g) indicate the presence of nanocrystals, whereas no speckles are detected in (f,k). (m) HAADF-STEM image and elemental mapping results of the acid-treated FeNiPC MG showing the nanoscale chemical heterogeneities. Ni and P elements are majorly distributed in the dark region, whereas Fe and O are segregated in the bright region.

geneity present an amazing self-stabilizing behavior that enables them to retain a high efficiency of 100% even after 40,000 s testing in the electrocatalytic process.[23] The synergistic effect and the amorphous structure of an $Ir_{25}Ni_{33}Ta_{42}$ MG nanofilm provide large amounts of active sites that extremely promote the electrochemical activity.[24] A $Ni_{40}Zr_{40}Ti_{17}Pt_3$ MG ribbon with a honeycombed nanoporous/glassy sandwich structure and a slight lattice distortion exhibits a small overpotential and a low Tafel slope in the HER.[25] An $Al_{80}Ni_6Co_3Mn_3Y_5Au_3$ MG ribbon is able to self-construct a protective Au-rich interface during the catalytic process that greatly enhances the long-term stability.[26] Moreover, our recent reports found that the $Fe_{78}Si_9B_{13}$ MG with a long-range disordered structure presents enhanced catalytic activity compared to the counterparts with more crystalline phases, which owing to the amorphous structure could provide a high density of unsaturated atomic coordination.[27] While the MGs present a rejuvenated catalytic behavior when annealed at the full crystallization temperature region, the corresponding catalytic performance is still lower than that of the initial MG with the amorphous structure.[28] It was also found that the microalloying of P elements into Fe-based MG could lead to an alteration of the atomic configuration and an optimization of electronic delocalization that greatly enhances the catalytic performance.[29] Furthermore, due to the superiority of the multicomponent nature, the MG catalysts are also widely regarded as templates for dealloying to fabricate nanoporous electrodes, such as the Pd−Ni−P,[30] Pd−Cu−Ni,[31] Pt−Ni−Cu−P,[11] and Au−Cu−Si[32] MGs. Nevertheless, it is noteworthy that most of the developed MG catalysts still require alloying noble metals to achieve efficient electrochemical reactions and generally perform well at the laboratory scale. In this regard, further regulation of the MG structure and composition will be a great demand to improve the corresponding water-splitting performance.

In this work, inspired by both the characteristics of the multicomponent amorphous structure and unique structural and chemical heterogeneities, a flexible freestanding MG ribbon (Figure 1a) with an atomic composition of $Fe_{50}Ni_{30}P_{13}C_7$ was developed as a bifunctional electrode for efficient water electro-splitting in alkaline media. We initially employed a simple acid-etching process to achieve surface hydroxylation of the ribbon. The surface structure was then self-constructed to structural and chemical heterogeneities on a nanoscale that played an essential role in the fabulous water-splitting performance. Furthermore, density functional theory (DFT) calculations revealed that those heterogeneities were the origin of the superior activities of water splitting, that is, the

https://doi.org/10.1021/acsami.1c22294
ACS Appl. Mater. Interfaces 2022, 14, 10288−10297

self-constructed amorphous FeOOH was a favorable microstructure to optimize the rate-determining step (RDS) in the water oxidation process and the amorphous/crystalline Ni_2P made a major contribution to the stabilization of the hydrogen proton (H*) adsorption/desorption in HER, respectively.

MATERIALS AND METHODS

Materials Preparation. MG ribbons, with nominal atomic compositions of $Fe_{50}Ni_{30}P_{13}C_7$ and $Fe_{80}P_{10}C_{10}$, were prepared by our previously reported melt-spinning technique.[33] Typically, master alloy ingots (~20 g) were initially fabricated by mixing and melting Fe_3P, Fe_3C, and Ni_3P granules via an arc-melting technique under an argon (Ar) atmosphere protection. The master ingots were then cut into small pieces to be filled into a quartz crucible and re-melted in a temperature range of 1200−1500 °C under an Ar atmosphere protection. The melted alloy liquids were immediately ejected onto a rotated copper (Cu) wheel surface (~30 m s^{-1}) to rapidly quench to room temperature. Afterward, the prepared freestanding MG ribbons with an approximate thickness of ~20 μm were further cut into 0.2 × 2 cm^2 (Figure 1a) for the purpose of working electrodes throughout in this work. With respect to the acid-etching process, the as-spun $Fe_{50}Ni_{30}P_{13}C_7$ MG ribbons were immersed in a HNO_3 solution for 5 min. The treated and used MG ribbons were ultrasonicated four times and preserved in an absolute ethanol solution for the subsequent experiments/characterizations.

Materials Characterization. Characterization of the surface morphology was carried out using scanning electron microscopy (SEM) (JEOL JSM-820) equipped with energy-dispersive X-ray spectroscopy (EDS). Analysis of the spatial structure was conducted employing high-resolution transmission electron microscopy (HRTEM, JEOL TEM 2100F) coupled with a selected area electron diffraction (SAED) and the EDS. Structural characterization was also measured by an X-ray diffraction (XRD, Rigaku) instrument (Cu Kα radiation). Surface chemical valence was characterized by an X-ray photoelectron spectrometry (XPS) (VG ESCALAB 220i-XL) with Al Kα radiation as the excitation source. All these characterization techniques were employed for the as-spun, acid treated, and used MG ribbons throughout in this work. The specific atomic composition of the as-spun $Fe_{50}Ni_{30}P_{13}C_7$ MG was identified by inductively coupled plasma-optical emission spectroscopy (ICP-OES, SPECTROBLUE). The as-spun $Fe_{50}Ni_{30}P_{13}C_7$ MG was completely dissolved in aqua regia prior to the ICP-OES measurement.

Electrochemical Measurements. Water electro-splitting activities were measured by a standard three-electrode electrochemical station (CHI 660E) in the O_2- and N_2-saturated 1.0 M KOH solutions, whereas a graphite rod was used as the counter electrode, a saturated calomel electrode (SCE) was employed as the reference, and the self-supported MG ribbons were directly utilized as the working electrode, respectively. With respect to the activity comparison, 2 mg of commercial Pt/C or IrO_2 nanoparticles (20 wt %, Sigma-Aldrich) were dispersed into a mixture solution that contained 10 μL of Nafion (5 wt %, Sigma-Aldrich) and 390 μL of water/ethanol solution (3:1, v/v) under 1 h of ultrasonication for the ink preparation. A glassy carbon electrode with a diameter of 5 mm and surface area of 0.196 cm^2 was then used for the ink loading (10 μL). A reversible hydrogen electrode (E vs RHE) based on the Nernst equation was employed to calibrate the measured potentials (iR loss correction applied). The linear sweep voltammetry with a scan rate of 5 mV s^{-1} was applied to measure the polarization curves of the MG ribbons. A chronoamperometry method was employed for the stability testing at 20 mA cm^{-2} in 1.0 M KOH solution. The frequency range of the electrochemical impedance spectroscopy (EIS) was between 0.1 to 10^5 Hz. The measurement of the double-layer capacitance (C_{dl}) and the calculation of the electrochemical surface area (ECSA) were according to our previous work.[34] The specific capacitance (C_s) value was assumed to be 0.04 mF cm^{-2} owing to the flat surface of the MG ribbons.[25,35]

DFT Simulations. DFT method was employed using the Cambridge Sequential Total Energy Package (CASTEP) module in Materials Studio to calculate the overall water-splitting behaviors of our acid-treated MG ribbons. The generalized gradient approximation method with the Perdew−Burke−Ernzerhof function (GGA-PBE) was utilized to describe the exchange and corrections of the atomic interactions. The ultrasoft pseudo-potential method was used to illustrate the interactions between the valence electrons and ionic cores. A plane-wave basis set with a cutoff energy of 400 eV was assigned. The Brillouin zone was sampled by a Monkhorst−Pack grid. The tolerances of energy, force, and displacement for the structure optimization were 10^{-6} eV $atom^{-1}$, 0.02 eV $Å^{-1}$, and 0.001 Å, respectively. The self-consistence field was set to 10^{-6} eV $atom^{-1}$. The effect of van der Waals interaction was considered by the semi-empirical DFT-D force-field approach.[36] Three representative atomistic models, including crystalline Ni_2P, amorphous Ni_2P, and amorphous FeOOH, were constructed based on our experimental characterization to investigate their overall water-splitting behaviors. The atoms in amorphous Ni_2P and FeOOH were randomly assigned. Structure relaxation was conducted at room temperature with periodic boundary conditions under the canonical ensemble (NVT). The geometry optimization of the amorphous models was then achieved for the investigation of electrocatalytic behaviors in this work. A vacuum gap of ~20 Å was employed to create free surface for the simulation of overall water-splitting behaviors for all the models. The k points for Ni_2P were set to be 3 × 3 × 1, and an Γ point was used for amorphous Ni_2P and FeOOH to sample the Brillouin zone.

OER calculations in alkaline media were performed according to previously reported procedures. The reaction free energy of adsorbates in the OER process was obtained by a geometry optimization of intermediates. Four electron-transfer steps were considered for the OER activity, which were (1) the hydroxide ions were dissociated into OH* and absorbed onto a catalyst surface; (2) the reaction between OH* and hydroxide ions was occurred to form O* and water molecules; (3) the reaction between O* and hydroxide ions was occurred to produce OOH*; and (4) the OOH* reacted with hydroxide ions to produce O_2. The Gibbs free energies of the hydrogen adsorption (ΔG_{H^*}) were calculated based on the equation: $\Delta G_{H^*} = \Delta E_{H^*} + \Delta ZPE - T\Delta S$, whereas the ΔE_{H^*}, ΔZPE, T, and ΔS represent the binding energy, zero-point energy change, temperature, and entropy change of the H adsorption system, respectively. The entropy vibration of H adsorption at the adsorbed states was negligible. Thus, ΔS was obtained from the following equation: $\Delta S = S_{H^*} - \frac{1}{2}S_{H_2} \approx -\frac{1}{2}S_{H_2}$, whereas S_{H_2} is the entropy of H_2 in the gas phase at the standard conditions. Besides, ΔZPE was calculated from the equation: $\Delta ZPE = ZPE_{H^*} - \frac{1}{2}ZPE_{H_2}$. Therefore, the free energy of the adsorbed state was calculated using the simplified equation of $\Delta G_{H^*} = \Delta E_{H^*}$+0.24 eV.[37] The water adsorption energies (ΔE_{H2O}) at the surface of catalysts were calculated by the equation: $E_{H_2O} = E_{surf+H_2O} - E_{surf} - E_{H_2O}$, whereas the E_{surf} and E_{surf+H_2O} are the total energies of the surface before and after water adsorption and E_{H_2O} is the energy of a free water molecule.

RESULTS AND DISCUSSION

Structural Characterization. Figure 1b shows the schematic illustration and the evolution of the surface structure during the nitric acid etching process, in which the as-spun FeNiPC MG ribbon was employed as a precursor. It is noteworthy that the original surface of the as-spun MG was ultra-smooth and at an acid-treatment time of 5 min, the surface morphology was evolved to a microplate-like morphology. The amorphous structure of the as-spun MG was confirmed by the HRTEM image and the corresponding SAED pattern (Figure S1). Figure S2 shows a STEM image with elemental mapping results and EDS analysis of the as-spun MG. It is clear that the four components of Fe, Ni, P, and C were homogeneously distributed in the amorphous matrix, while the observed atomic composition was very close to the

https://doi.org/10.1021/acsami.1c22294
ACS Appl. Mater. Interfaces 2022, 14, 10288−10297

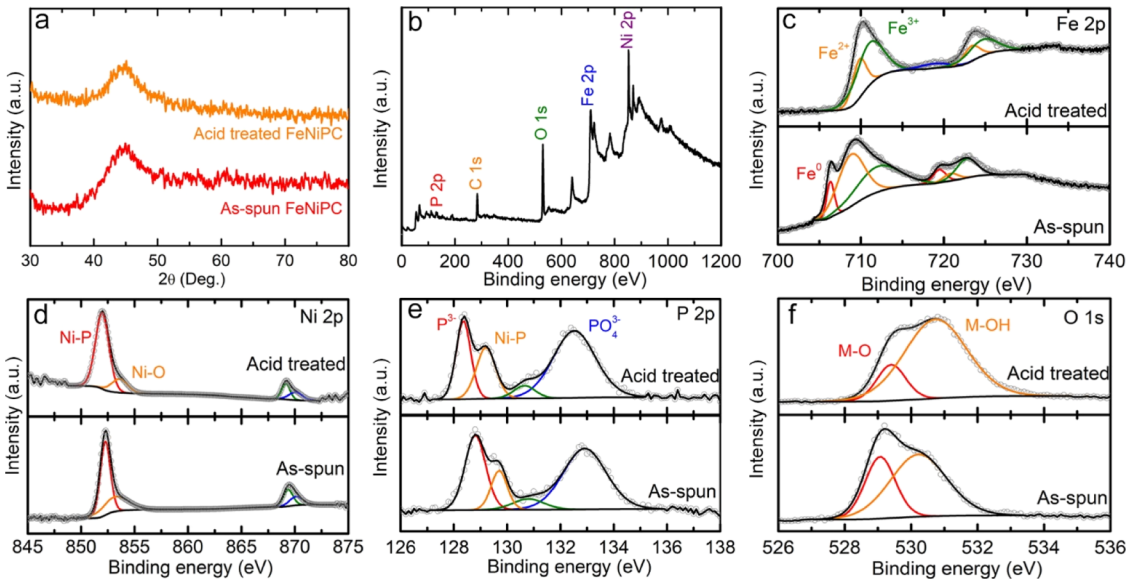

Figure 2. Spectral analysis. (a) XRD patterns of the as-spun and acid-treated FeNiPC MGs. (b) Full XPS spectrum of the acid-treated FeNiPC MG. High-resolution XPS profiles of (c) Fe 2p, (d) Ni 2p, (e) p 2p, and (f) O 1s for the as-spun and acid-treated FeNiPC MGs.

theoretical value of the $Fe_{50}Ni_{30}P_{13}C_7$. To further accurately identify the specific composition, we also carried out the ICP-OES measurement of the $Fe_{50}Ni_{30}P_{13}C_7$ MG (Table S1). Note that the quantification of the C element using an ICP-OES technique is not achievable. Nevertheless, the measured atomic ratio of Fe/Ni/P was 54:34:12, which was also approaching their theoretical atomic ratio of 54:32:14. The EDS result of the MG surface acquired from the SEM image was also similar to the theoretical design (Figure S3). To emphasize the chemical synergistic function of the quaternary FeNiPC MG, we also prepared a ternary MG ribbon with the chemical composition of $Fe_{80}P_{10}C_{10}$ for a performance comparison. The corresponding characterization results of its amorphous structure, smooth surface morphology, and atomic compositions in the matrix and on the surface are shown in Figures S4–S7.

Figure 1c–m presents the microstructural evolution of the FeNiPC MG at an acid-treated time of 5 min. Figure 1c,h exhibits typical HRTEM images at the topmost layer of the acid-treated FeNiPC MG, indicating that the structure was majorly amorphous. Nevertheless, it is worthwhile that the regions at A and C in Figure 1c,h represented clear local atomic orderings. The corresponding magnified areas (Figure 1d,i) indicate that such an ordered atomic arrangement was assigned to nanocrystals with an average size of ∼2 nm and an average lattice space fringe of ∼0.205 nm, which was in agreement with the (021) plane of a crystalline Ni_2P phase.[38] Fast Fourier transform (FFT) patterns of the corresponding areas in Figure 1e,j presented obvious bright spots on the diffuse ring, further corroborating the presence of the nanocrystals. In contrast, the magnified regions at B and D and their corresponding FFT patterns exhibited an apparent disordered atomic structure and amorphous diffraction halo, indicating that these areas were mainly in the amorphous structure (Figure 1f,g,k,l). Figures 1m and S8 show HAADF-STEM images and the elemental mapping results of the acid-treated FeNiPC MG. It was found that the elements of Ni and P were majorly distributed in the dark region, while the elements of Fe and O were mainly concentrated in the bright region. To further quantitively identify the atomic percentages on those dark and bright regions, EDS analysis is employed, as shown in Figure S9. The atomic ratio of Ni/P at the dark region was 24/11 and this value was very close to the above-mentioned Ni_2P phase, further verifying the presence of Ni_2P in the dark region. Moreover, considering the area B in Figure 1f is in an amorphous structure, it suggested that the dark region of the acid-treated FeNiPC MG contained both the crystalline and amorphous Ni_2P phases. With respect to the atomic ratio at the bright region, it was found that the Fe/O ratio was 19/55 with extremely weak signals of Ni and P. Accordingly, combining the structural analysis at region D in Figure 1k, the bright region of the acid-treated FeNiPC MG would mainly include the amorphous FeOOH (acid-treated process in a water-based environment) and tiny amounts of Fe/Ni oxides. Therefore, the findings of the structural characterizations revealed that the topmost layer of the acid-treated FeNiPC MG presented structural and chemical heterogeneities under the nanoscale and the major active sites contributing to the water-splitting activity would be crystalline Ni_2P, amorphous Ni_2P, and amorphous FeOOH, respectively (details in the following DFT simulations).

The amorphous structure of the as-spun and acid-treated FeNiPC MG was further confirmed by XRD in Figure 2a. It is noteworthy that a broad diffuse diffraction peak was obtained for the acid-treated FeNiPC MG without the observation of the crystalline phase of Ni_2P, which was owing to the fact that the size of the nanocrystals was on the ∼2 nm scale that was not sensitive to the XRD detection.[34] Figure 2b–f show XPS results of the as-spun and acid-treated FeNiPC MG. The binding energies of Fe 2p, Ni 2p, P 2p, and O 1s with strong intensities were observed in the full range XPS spectrum of the FeNiPC MG surface (Figure 2b). Because the binding energy of C 1s located at 284.8 eV is employed normally to calibrate samples, the analysis of the specific chemical compositions and C 1s by the XPS method was not included in this work. Figure 2c presents the high-resolution XPS spectra of Fe 2p for the as-spun and acid-treated FeNiPC MG. Three major peaks at the binding energies of 707.0, 709.5, and 713.0 eV, which correspond to metallic Fe (Fe^0), Fe^{2+}, and Fe^{3+}, respectively, were clearly detected on the as-spun FeNiPC MG. In

https://doi.org/10.1021/acsami.1c22294
ACS Appl. Mater. Interfaces 2022, 14, 10288−10297

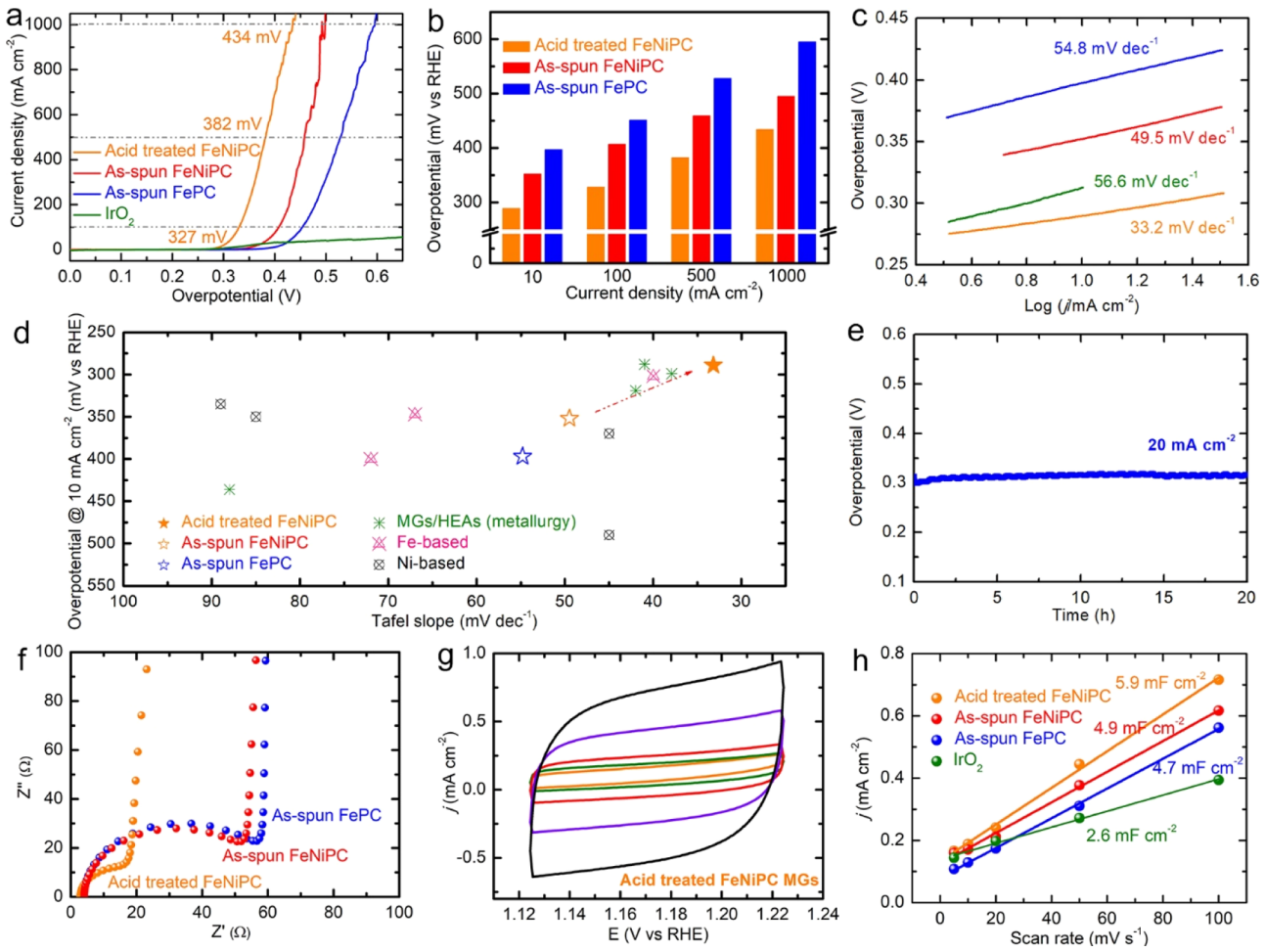

Figure 3. Water oxidation performance in 1.0 M KOH solution. (a) OER polarization curves of the ribbon samples at a scan rate of 5 mV s^{-1} with *iR* loss correction. (b) Achieved overpotentials of the ribbon samples at different current densities. (c) Tafel slopes. (d) Comparison of OER activity with recently reported transition-metal-based electrocatalysts in 1.0 M KOH solution. (e) OER stability performance of the acid-treated FeNiPC MG over 20 h at a current density of 20 mA cm^{-2}. (f) EIS measurements of the MGs. (g) Cyclic voltammetry curves measured at various scan rates in the range of 5−100 mV s^{-1}. (h) Capacitive currents plotted against a scan rate at 0.15 V versus RHE for the IrO_2, as-spun, and acid-treated MGs.

comparison, only two peaks at the binding energies of 710.0 and 712.4 eV were observed on the acid-treated FeNiPC MG. Such results suggest that the Fe^0 on the as-spun FeNiPC MG was gradually evolved into Fe^{2+} and Fe^{3+} during the acid-treated process that finally led to the formation of Fe oxides and FeOOH, respectively.[35] The Ni 2p XPS spectra of the as-spun and acid-treated MGs exhibited peaks at 852.3 and 854.0 eV that could be assigned to the compounds of Ni−P and Ni−O, respectively[39] (Figure 2d). It is noted that the concentration of Ni−P (integral area) for the acid treated MG was obviously higher than that for the as-spun MG, which is owing to the chemical heterogeneities on the acid-treated ribbon surface (Figures 1c−m and S8, and S9). The P 2p XPS spectra consisted of three major peaks at 128.8, 129.8, and 132.9 eV, which were ascribed as P^{3-}, Ni−P, and PO_4^{3-}, respectively.[34,39] Such results further evidenced the formation of the Ni_2P phase (Figure 2e). The O 1s XPS spectra showed two peaks that could be assigned as metal oxides and metal hydroxides with the binding energies of 529.0 and 530.5 eV, respectively (Figure 2f). Interestingly, it is noteworthy that the Fe 2p and O 1s spectra exhibited a positive shift, while the Ni 2p and P 2p presented a negative shift compared to those of the as-spun ribbon, suggesting that the Fe sites would be the hydroxyl acceptors[40] and most of the Ni sites would be coordinated with the P sites to form the NiP phase, which is in good agreement with the HRTEM characterizations in Figures 1c−m and S8. Moreover, due to the high atomic diffusion rate of the MG,[25] the acid-treated process would enhance the atomic re-arrangement that led to the structural and chemical heterogeneities on the surface. It may give rise to an increased concentration of Ni−P and FeOOH species and a robust electron hybridization phenomenon for the improvement of the following electrocatalytic performance.[25]

Electrocatalytic Activity. The prepared flexible free-standing MG ribbons were employed directly as the working electrodes for the investigation of water oxidation activity in the 1.0 M KOH solution. Figure 3a shows the OER polarization curves of the MG ribbons at a scan rate of 5 mV s^{-1} with *iR* loss corrections. The overpotential of the as-spun FeNiPC MG at a current density of 10 mA cm^{-2} was 352 mV, which was much lower than that of the as-spun FePC MG, suggesting the synergistic function of Fe and Ni elements to an enhanced OER activity. When the acid-treated process applied, it was found that the overpotential of the FeNiPC MG with the nanoscale heterogeneities presented a sharp decrease to 289 mV, and this value was much lower than that of the

https://doi.org/10.1021/acsami.1c22294
ACS Appl. Mater. Interfaces 2022, 14, 10288−10297

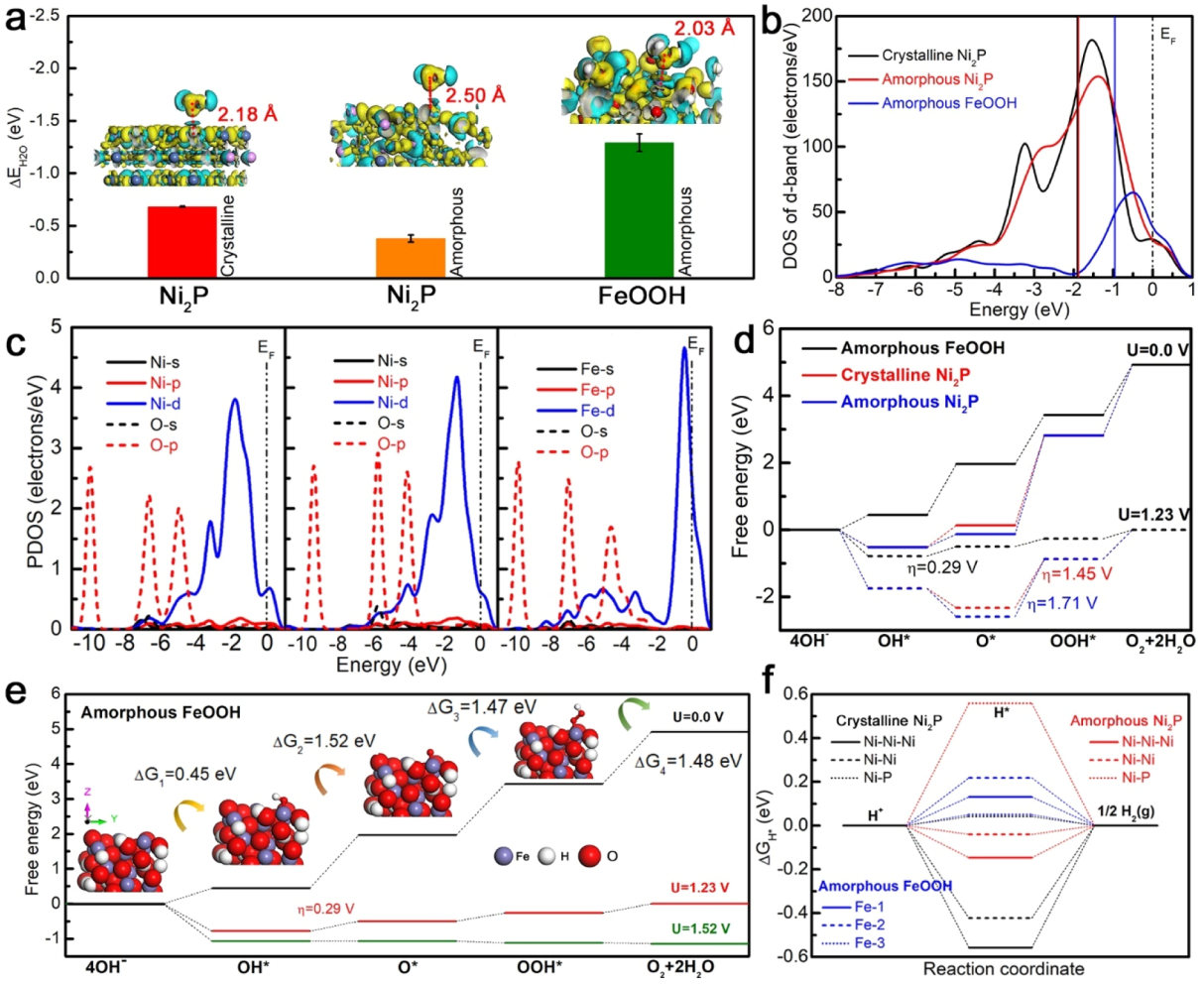

Figure 4. DFT simulation. (a) DFT calculation of ΔE_{H_2O} on the exposed surfaces of crystalline Ni_2P, amorphous Ni_2P, and amorphous FeOOH. The insets show the electron density differences (cyan and yellow isosurfaces represent the depletion and segregation of electrons, respectively). (b) d-Orbital partial density of states (*d*-PDOS) and (c) PDOSs of the three models. Free energy profiles of the (d) three models at $U = 0$ and 1.23 V and (e) amorphous FeOOH at $U = 0$, 1.23, and 1.52 V. The insets present the relaxed configurations of the initial and intermediate structures with the adsorption of OH*, O*, and OOH* onto the amorphous FeOOH. (f) Gibbs free energy (ΔG_{H^*}) profiles on various catalytic sites at the surfaces.

commercial IrO_2 particles (320 mV). More importantly, it is noteworthy that such acid-treated MGs only require the overpotentials of 327, 382, and 434 mV to drive the industrial-level current densities of 100, 500, and 1000 mA^{-2}, respectively, demonstrating their promoted water oxidation performance than those of the as-spun MGs and other reports (Figure 3b).[41−43] The fast oxygen gas evolution on the acid-treated FeNiPC MG anode at a current density of 500 mA cm^{-2} is shown in Movie S1. Furthermore, the corresponding Tafel slope value of the acid-treated FeNiPC MG was achieved to ~33.2 mV dec^{-1} (Figure 3c), which was also remarkably lower than those of the as-spun MGs and the IrO_2 electrocatalysts (49.5, 54.8, and 56.6 mV dec^{-1} for as-spun FeNiPC, as-spun FePC, and IrO_2, respectively). Such results demonstrate that faster kinetics were achieved for the acid-treated FeNiPC MG, resulting in a higher water oxidation activity. Figure 3d and Table S2 show the OER performance comparison with the recently reported state-of-the-art electrocatalysts, such as the MG or high-entropy alloy ribbons produced by the metallurgical method, and Fe- and Ni-based electrocatalysts prepared by wet chemistry methods, further elucidating the superior water oxidation activity of our acid-treated FeNiPC MG. Figure 3e shows the OER stability of the acid-treated FeNiPC MG that was recorded by a chronoamperometry method at the current density of 20 mA cm^{-2}. It manifests that our FeNiPC MG ribbons can survive over 20 h without an obvious overpotential amplification during the OER measurement. In addition, the corresponding structural characterizations of the used FeNiPC MG were also carried out to further highlight their strong stability, such as the SEM images and EDS result for the surface structure in Figure S10, the XRD pattern for the structural analysis in Figure S11, and the high-resolution XPS spectra for the analysis of the surface chemical states in Figure S12, respectively. Note that the XRD result of the used FeNiPC MG exhibited a broad diffuse diffraction peak, indicating that the structure of the used ribbons mainly retained in the amorphous state. The tiny trace of nanocrystals was ascribed to the formation of α-FeOOH[44] and Ni_2P.[45] Moreover, it was found that the Ni−P concentration of the used MG sample was sharply decreased (Figure S12c), while the binding energy of M−O and M−OH exhibited a positive shift (Figure S12d), compared to those of the acid-treated sample (Figure 2e,f). This result suggested the formation of Ni oxides, which was inevitable during oxygen

https://doi.org/10.1021/acsami.1c22294
ACS Appl. Mater. Interfaces 2022, 14, 10288−10297

production activity. Furthermore, the P^{3-} with a binding energy of 128.8 eV was also invisible after the OER testing, indicating the P^{3-} site was transformed into the PO_4^{3-} (Figure S12c). Figure 3f shows EIS measurements of the samples in the 1.0 M KOH solution. A smaller semicircle diameter was obtained for the acid-treated FeNiPC MGs compared to those of the as-spun FeNiPC and FePC MGs, indicating their stronger electron-transfer ability.[46] The C_{dl} are carried out by a cyclic voltammetry method in Figures 3g and S13. It was found that the C_{dl} value of the acid-treated FeNiPC MG was 5.9 mF cm^{-2}, which was slightly higher than those of the as-spun FeNiPC and FePC MGs as well as the IrO_2 electrocatalysts (4.9, 4.7, and 2.6 mF cm^{-2}). Moreover, the calculated ECSA values of the samples also presented the same trend with the obtained C_{dl} values (Figure S14). To highlight the intrinsic activity of the electrocatalysts, the OER polarization curves were further normalized by ECSA values of the prepared samples and IrO_2 at a scan rate of 5 mV s^{-1} (Figure S15). The achieved overpotential of the acid-treated FeNiPC MG was much lower than those of the as-spun MGs and IrO_2, indicating that the surface hydroxylation process of the MG led to an improved number of active sites that finally enhance the reaction kinetics.

With respect to the HER performance, our prepared acid-treated FeNiPC MG also exhibited excellent activities compared to those of the as-spun MGs and the benchmark Pt/C nanoparticles (Figure S16). As shown in Figure S16a, the overpotential of the acid-treated FeNiPC MG was 113 mV at a current density of 10 mA cm^{-2}, outperforming those of the as-spun MGs (143 and 262 mV for the as-spun FeNiPC and as-spun FePC ribbons). While the HER activity of the acid-treated FeNiPC MGs cannot surpass that of the benchmark Pt/C nanoparticles (33 mV), their much lower materials cost still presented great potential in actual applications. Moreover, the resulting HER Tafel slope of the acid-treated FeNiPC MG achieved was 40.6 mV dec^{-1} (Figure S16b), which was also significantly promoted than those of the as-spun MGs and close to the value of Pt/C nanoparticles (59.7, 98.5, and 31.2 mV dec^{-1} for the as-spun FeNiPC, as-spun FePC, and Pt/C particles, respectively). It manifests that their faster HER kinetics were according to the Volmer–Heyrovsky mechanisms. Movie S1 presents the overall water-splitting performance when using the acid-treated FeNiPC MGs as both the anode and cathode. The achieved cell voltage is 1.59 V driving the current density of 10 mA cm^{-2}, which is comparable to those of the state-of-the-art electrocatalysts (Figure S17). Furthermore, the acid-treated FeNiPC MG also presented a great HER stability over 20 h at a current density of 20 mA cm^{-2} in the alkaline condition, although a slight overpotential amplification of only ~10 mV was observed (Figure S16c).

DFT Simulations. To reveal the origin of the excellent water-splitting activities, DFT calculations were conducted to achieve an atomic-scale understanding of our acid-treated FeNiPC MG. Particularly, according to the nanoscale heterogeneities unveiled from our above characterizations, three representative atomic models, including crystalline Ni_2P, amorphous Ni_2P, and amorphous FeOOH, were built to investigate their water-splitting performance. It is well accepted that the very beginning step of the water-splitting reaction is the adsorption of H_2O in alkaline media.[47] Accordingly, the ΔE_{H2O} of various active sites exposed at the surface are calculated in Figure 4a. It was found that the amorphous FeOOH exhibited the highest ΔE_{H2O} value of −1.29 eV and its preferable adsorption site was the Fe atom (Figure S17c). In comparison, the ΔE_{H2O} values of the crystalline and amorphous Ni_2P were −0.68 and −0.38 eV, respectively, in which the Ni atoms were the active adsorption sites (Figure S17a,b). The Figure 4a inset presents electron density differences after the H_2O adsorbed onto the three models. Typically, the interaction between the amorphous FeOOH and H_2O presented the strongest charge transferability, followed by that between the crystalline Ni_2P and H_2O, and the interaction between the amorphous Ni_2P and H_2O exhibited the weakest charge transferability. Moreover, it is noteworthy that the calculated equilibrium distances were 2.18, 2.50, and 2.03 Å for the active sites of crystalline Ni_2P, amorphous Ni_2P, and amorphous FeOOH, respectively. The sequence of such interatomic distances was also consistent with the H_2O adsorption ability, demonstrating the shorter equilibrium distance it possessed the stronger H_2O adsorption ability. To further reveal the effect of binding strengths, the *d*-band center and partial density of states (PDOS) between the H_2O and the three models are calculated in Figure 4b,c. As shown in Figure 4b, the *d*-band center of the amorphous FeOOH was much closer to the Fermi level (E_F) compared to that of the crystalline and amorphous Ni_2P. Moreover, the electronic interaction between the d-orbital of Fe and the p-orbital of O for the amorphous FeOOH was much stronger than that between the d-orbital of Ni and the p-orbital of O for both the crystalline and amorphous Ni_2P (Figure 4c). Such results indicate that the amorphous FeOOH played a primary contribution to the H_2O adsorption step.

With regard to the OER activity, relaxed configurations of the three models and their corresponding intermediate structures with the adsorptions of OH*, O*, and OOH* are shown in the Figures S18–20 and 4e inset. Figure 4d shows the free energy profiles of the OER process of the three models at zero and equilibrium potentials (U = 0.0 V and U = 1.23 V) (detailed results in Table S3). It was found that the RDS of the OER process for the amorphous FeOOH was the transition from OH* to O*, whereas the RDS for both crystalline and amorphous Ni_2P was the transition from O* to OOH*. The results show that the free energy (ΔG_2) was ~1.52 eV with a relevant theoretical overpotential (η) value of 0.29 V for the amorphous FeOOH. In comparison, the free energies (ΔG_3) for the crystalline and amorphous Ni_2P were achieved at 2.68 and 2.94 eV with the η values of 1.45 and 1.71 V, respectively (detailed results in Table S4). The lower overpotential required for the amorphous FeOOH revealed that it was the dominant atomic configuration that led to the outstanding OER performance. Furthermore, when the overpotential increased to 1.52 V, all the elementary reaction steps of the amorphous FeOOH were achieved as downhills (Figure 4e). Moreover, it was observed that the moderate binding energies of OH*, O*, and OOH* at the active sites of the amorphous FeOOH were beneficial to low overpotentials, although the interaction between OH* and the active sites was slightly stronger than that of O* and OOH*. However, it is worthwhile that the calculated value of ΔG_{OH*} was positive, which was able to mitigate the uphill formation of the subsequent O*. Conversely, the negative values of ΔG_{OH*} for the crystalline and amorphous Ni_2P as well as the negative value of ΔG_{O*} for amorphous Ni_2P resulted in very strong interactions for OH* and O* intermediates, which caused the uphill formation of the subsequent OOH* intermediate.[48] To gain insights into the physical mechanisms, local electron

https://doi.org/10.1021/acsami.1c22294
ACS Appl. Mater. Interfaces 2022, 14, 10288–10297

density differences between the O atom in OH*, O*, and OOH*, and the active sites in the three models are further analyzed in Figures S21–S23. It was found that an intensive electron transfer was occurred from Ni atoms to the O atom in the O* intermediate, while it was extremely weak in the OOH* intermediate, for both the crystalline and amorphous Ni_2P. On the other hand, the intensity of electron transfer from the Fe atom to the O atom for the amorphous FeOOH showed a trend of OOH* > O* > OH*. Because the RDSs of the crystalline and amorphous Ni_2P were determined by $\Delta G_3 = \Delta G_{OOH^*} - \Delta G_{O^*}$ and the RDS of amorphous FeOOH was determined by $\Delta G_2 = \Delta G_{O^*} - \Delta G_{OH^*}$, the negative OER performance of the crystalline and amorphous Ni_2P was primarily attributed to the weak electron-transfer ability of the catalytic sites toward OOH*. Nevertheless, the gradual increase of the interaction intensity between the catalytic sites and intermediates was favorable for the OER activity with the ongoing reaction steps in the alkaline solution. Hence, the DFT results demonstrated that the amorphous FeOOH would be the most beneficial configuration for the OER activity in this work, which is in great accordance with other reports.[49]

It is well accepted that the Gibbs free energies of the ΔG_{H^*} is normally considered as a key descriptor of the HER performance under alkaline conditions. Typically, the HER activity is promoted when the value of ΔG_{H^*} approaches zero because the HER process includes the reversible adsorption and desorption of H*, which requires a moderate energy for the interaction between the catalytic sites and H*.[37,50] In this regard, to unveil the HER mechanisms, the values of ΔG_{H^*} were probed after the H* adsorbed onto various local coordination environments of the three atomistic models (Figures S24–S26). The Fe atom in the amorphous FeOOH and the Ni–Ni bridge, Ni–P bridge, and Ni–Ni–Ni hollow sites in the crystalline and amorphous Ni_2P were accounted as the active sites for the H* adsorption throughout the HER activity. Figure 4f shows the details of the ΔG_{H^*} profiles on various catalytic sites. It was found that six catalytic sites performed excellent ΔG_{H^*} values less than ±0.20 eV, in which three of them presented outstanding ΔG_{H^*} values less than ±0.10 eV, suggesting a significant contribution of the structural heterogeneities in our MG ribbon to the HER activity.

CONCLUSIONS

In summary, a self-supported flexible MG ribbon with an atomic composition of $Fe_{50}Ni_{30}P_{13}C_7$ was successfully developed by a large-scalable melt-spinning technique. After a simple surface hydroxylation process, the MG ribbon evolved into unique structural and chemical heterogeneities that exhibited outstanding industrial-level water oxidation performance in the 1.0 M KOH solution, that is, the achieved overpotentials at current densities of 100, 500, and 1000 mA cm^{-2} were 327, 382, and 434 mV, respectively, while maintaining a reliable performance for 20 h with a negligible structural deterioration. Combined with the experimental characterizations and DFT calculations, the fabulous water-splitting performance of the acid-treated MG ribbon was majorly owing to the structural heterogeneity that possessed various active sites including amorphous FeOOH, amorphous Ni_2P, and crystalline Ni_2P, which enable regulating the electronic structure and optimizing each RDS during oxygen evolution activity. Our findings are anticipated to provide a new strategy for the development of cost-effective, flexible, and freestanding MG that can be directly employed as bifunctional electrodes in the water electro-splitting application. Furthermore, it uncovers a new paradigm to build the relationship between the heterogeneities in MG and electrocatalytic performance that can help to better understand the mechanisms behind other potential electrode materials.

ASSOCIATED CONTENT

Supporting Information

The Supporting Information is available free of charge at https://pubs.acs.org/doi/10.1021/acsami.1c22294.

Structural information of as-spun FeNiPC MGs, as-spun FePC MGs, and acid-treated FeNiPC MGs, characterizations of the used MGs, cyclic voltammetry curves, ECSA results, OER normalized by ECSA, HER activities, DFT calculations and atomistic models, ICP-OES results, HER and OER performance comparison, calculated free energies of the transient states, and energy variations for OER electrochemical steps (PDF)

Fast oxygen gas evolution on the acid-treated FeNiPC MG anode (MP4)

AUTHOR INFORMATION

Corresponding Authors

Ligang Sun − *School of Science, Harbin Institute of Technology, Shenzhen 518055, China*; Email: sunligang@hit.edu.cn

Tao Yang − *Department of Materials Science and Engineering, City University of Hong Kong, Hong Kong SAR 00000, China*; Email: taoyang6-c@my.cityu.edu.hk

Baolong Shen − *School of Materials Science and Engineering, Jiangsu Key Laboratory for Advanced Metallic Materials, Southeast University, Nanjing 211189, China*; orcid.org/0000-0002-0358-6540; Email: blshen@seu.edu.cn

Authors

Zhe Jia − *School of Materials Science and Engineering, Jiangsu Key Laboratory for Advanced Metallic Materials, Southeast University, Nanjing 211189, China*; orcid.org/0000-0002-5063-8390

Yilu Zhao − *School of Materials Science and Engineering, Harbin Institute of Technology, Shenzhen 518055, China*

Qing Wang − *Laboratory for Microstructures Institute of Materials Science, Shanghai University, Shanghai 200072, China*

Fucong Lyu − *Department of Materials Science and Engineering, City University of Hong Kong, Hong Kong SAR 00000, China*; orcid.org/0000-0002-8060-2372

Xiaobao Tian − *Department of Mechanics, Sichuan University, Chengdu 610065, China*

Shun-Xing Liang − *School of Engineering, Edith Cowan University, Perth, Western Australia 6027, Australia*

Lai-Chang Zhang − *School of Engineering, Edith Cowan University, Perth, Western Australia 6027, Australia*; orcid.org/0000-0003-0661-2051

Junhua Luan − *Department of Materials Science and Engineering, City University of Hong Kong, Hong Kong SAR 00000, China*

Qianqian Wang − *School of Materials Science and Engineering, Jiangsu Key Laboratory for Advanced Metallic Materials, Southeast University, Nanjing 211189, China*

Complete contact information is available at: https://pubs.acs.org/10.1021/acsami.1c22294

https://doi.org/10.1021/acsami.1c22294
ACS Appl. Mater. Interfaces 2022, 14, 10288−10297

Notes

The authors declare no competing financial interest.

■ ACKNOWLEDGMENTS

This work was supported by the National Natural Science Foundation of China: NSFC 51871140; the National Natural Science Foundation of China: NSFC 12002108; Guang Dong Basic and Applied Basic Research Foundation (grant no: 2020A1515110236); Science, Technology and Innovation Commission of Shenzhen Municipality (grant no: GXWD20201230155427003-20200824105236001); the Hong Kong Research Grant Council (grant no: CityU 21205621); the Department of Science and Technology, Guangdong Province (Grant No: 2020A1515110647); and the National Natural Science Foundation of China (grant no. 51631003).

■ REFERENCES

(1) Wei, Y.; Zou, P.; Yue, Y.; Wang, M.; Fu, W.; Si, S.; Wei, L.; Zhao, X.; Hu, G.; Xin, H. L. One-Pot Synthesis of B/P-Codoped Co-Mo Dual-Nanowafer Electrocatalysts for Overall Water Splitting. *ACS Appl. Mater. Interfaces* **2021**, *13*, 20024−20033.

(2) El-Refaei, S. M.; Russo, P. A.; Pinna, N. Recent Advances in Multimetal and Doped Transition-Metal Phosphides for the Hydrogen Evolution Reaction at Different pH values. *ACS Appl. Mater. Interfaces* **2021**, *13*, 22077−22097.

(3) Barati Darband, G.; Aliofkhazraei, M.; Hyun, S.; Shanmugam, S. Pulse Electrodeposition of a Superhydrophilic and Binder-Free Ni−Fe−P Nanostructure as Highly Active and Durable Electrocatalyst for Both Hydrogen and Oxygen Evolution Reactions. *ACS Appl. Mater. Interfaces* **2020**, *12*, 53719−53730.

(4) Huang, L.; Chen, D.; Luo, G.; Lu, Y. R.; Chen, C.; Zou, Y.; Dong, C. L.; Li, Y.; Wang, S. Zirconium-Regulation-Induced Bifunctionality in 3D Cobalt−Iron Oxide Nanosheets for Overall Water Splitting. *Adv. Mater.* **2019**, *31*, 1901439.

(5) Garcia-Torregrosa, I.; Wijten, J. H. J.; Zanoni, S.; Oropeza, F. E.; Hofmann, J. P.; Hensen, E. J. M.; Weckhuysen, B. M. Template-Free Nanostructured Fluorine-Doped Tin Oxide Scaffolds for Photoelectrochemical Water Splitting. *ACS Appl. Mater. Interfaces* **2019**, *11*, 36485−36496.

(6) Liu, B.; Huo, L.; Gao, Z.; Zhi, G.; Zhang, G.; Zhang, J. Graphene Decorated with Uniform Ultrathin (CoP)x−(FeP)1−x Nanorods: A Robust Non-Noble-Metal Catalyst for Hydrogen Evolution. *Small* **2017**, *13*, 1700092.

(7) Tee, S. Y.; Win, K. Y.; Teo, W. S.; Koh, L.-D.; Liu, S.; Teng, C. P.; Han, M.-Y. Recent Progress in Energy-Driven Water Splitting. *Adv. Sci.* **2017**, *4*, 1600337.

(8) Zhang, J.; Bai, X.; Wang, T.; Xiao, W.; Xi, P.; Wang, J.; Gao, D.; Wang, J. Bimetallic Nickel Cobalt Sulfide as Efficient Electrocatalyst for Zn−Air Battery and Water Splitting. *Nano−Micro Lett.* **2019**, *11*, 2.

(9) Zhang, S.; Wang, W.; Hu, F.; Mi, Y.; Wang, S.; Liu, Y.; Ai, X.; Fang, J.; Li, H.; Zhai, T. 2D CoOOH Sheet-Encapsulated Ni2P into Tubular Arrays Realizing 1000 mA cm−2-Level-Current-Density Hydrogen Evolution Over 100 h in Neutral Water. *Nano−Micro Lett.* **2020**, *12*, 140.

(10) Mukherjee, S.; Sekol, R. C.; Carmo, M.; Altman, E. I.; Taylor, A. D.; Schroers, J. Tunable Hierarchical Metallic-Glass Nanostructures. *Adv. Funct. Mater.* **2013**, *23*, 2708−2713.

(11) Doubek, G.; Sekol, R. C.; Li, J.; Ryu, W.-H.; Gittleson, F. S.; Nejati, S.; Moy, E.; Reid, C.; Carmo, M.; Linardi, M.; Bordeenithikasem, P.; Kinser, E.; Liu, Y.; Tong, X.; Osuji, C. O.; Schroers, J.; Mukherjee, S.; Taylor, A. D. Guided Evolution of Bulk Metallic Glass Nanostructures: A Platform for Designing 3D Electrocatalytic Surfaces. *Adv. Mater.* **2016**, *28*, 1940−1949.

(12) Jung, J.-W.; Ryu, W.-H.; Shin, J.; Park, K.; Kim, I.-D. Glassy Metal Alloy Nanofiber Anodes Employing Graphene Wrapping Layer: Toward Ultralong-Cycle-Life Lithium-Ion Batteries. *ACS Nano* **2015**, *9*, 6717−6727.

(13) Tao, K.; Qiao, J. C.; He, Q. F.; Song, K. K.; Yang, Y. Revealing the structural heterogeneity of metallic glass: Mechanical spectroscopy and nanoindentation experiments. *Int. J. Mech. Sci.* **2021**, *201*, 106469.

(14) Qiao, J. C.; Wang, Q.; Pelletier, J. M.; Kato, H.; Casalini, R.; Crespo, D.; Pineda, E.; Yao, Y.; Yang, Y. Structural heterogeneities and mechanical behavior of amorphous alloys. *Prog. Mater. Sci.* **2019**, *104*, 250−329.

(15) Wang, W. H. Dynamic relaxations and relaxation-property relationships in metallic glasses. *Prog. Mater. Sci.* **2019**, *106*, 100561.

(16) Li, H. X.; Lu, Z. C.; Wang, S. L.; Wu, Y.; Lu, Z. P. Fe-based bulk metallic glasses: Glass formation, fabrication, properties and applications. *Prog. Mater. Sci.* **2019**, *103*, 235−318.

(17) Orava, J.; Balachandran, S.; Han, X.; Shuleshova, O.; Nurouzi, E.; Soldatov, I.; Oswald, S.; Gutowski, O.; Ivashko, O.; Dippel, A.-C.; Zimmermann, M. v.; Ivanov, Y. P.; Greer, A. L.; Raabe, D.; Herbig, M.; Kaban, I. In situ correlation between metastable phase-transformation mechanism and kinetics in a metallic glass. *Nat. Commun.* **2021**, *12*, 2839.

(18) Tang, L.; Liu, H.; Ma, G.; Du, T.; Mousseau, N.; Zhou, W.; Bauchy, M. The energy landscape governs ductility in disordered materials. *Mater. Horiz.* **2021**, *8*, 1242−1252.

(19) Nomoto, K.; Ceguerra, A. V.; Gammer, C.; Li, B.; Bilal, H.; Hohenwarter, A.; Gludovatz, B.; Eckert, J.; Ringer, S. P.; Kruzic, J. J. Medium-range order dictates local hardness in bulk metallic glasses. *Mater. Today* **2021**, *44*, 48−57.

(20) Li, Z.; Huang, Z.; Sun, F.; Li, X.; Ma, J. Forming of metallic glasses: mechanisms and processes. *Mater. Today Adv.* **2020**, *7*, 100077.

(21) Fan, H.; Fan, Z.; Liu, X.; Lu, Z.; Ma, E. Atomic vibration as an indicator of the propensity for configurational rearrangements in metallic glasses. *Mater. Horiz.* **2021**, *8*, 2359−2372.

(22) Zhang, L.-C.; Jia, Z.; Lyu, F.; Liang, S.-X.; Lu, J. A review of catalytic performance of metallic glasses in wastewater treatment: Recent progress and prospects. *Prog. Mater. Sci.* **2019**, *105*, 100576.

(23) Hu, Y. C.; Wang, Y. Z.; Su, R.; Cao, C. R.; Li, F.; Sun, C. W.; Yang, Y.; Guan, P. F.; Ding, D. W.; Wang, Z. L.; Wang, W. H. A Highly Efficient and Self-Stabilizing Metallic-Glass Catalyst for Electrochemical Hydrogen Generation. *Adv. Mater.* **2016**, *28*, 10293−10297.

(24) Wang, Z. J.; Li, M. X.; Yu, J. H.; Ge, X. B.; Liu, Y. H.; Wang, W. H. Low-Iridium-Content IrNiTa Metallic Glass Films as Intrinsically Active Catalysts for Hydrogen Evolution Reaction. *Adv. Mater.* **2019**, *32*, 1906384.

(25) Li, R.; Liu, X.; Wu, R.; Wang, J.; Li, Z.; Chan, K. C.; Wang, H.; Wu, Y.; Lu, Z. Flexible Honeycombed Nanoporous/Glassy Hybrid for Efficient Electrocatalytic Hydrogen Generation. *Adv. Mater.* **2019**, *31*, 1904989.

(26) Ju, S.; Feng, J.; Zou, P.; Xu, W.; Wang, S.; Gao, W.; Qiu, H.-J.; Huo, J.; Wang, J.-Q. A robust self-stabilized electrode based on Al-based metallic glasses for a highly efficient hydrogen evolution reaction. *J. Mater. Chem. A* **2020**, *8*, 3246−3251.

(27) Jia, Z.; Duan, X.; Qin, P.; Zhang, W.; Wang, W.; Yang, C.; Sun, H.; Wang, S.; Zhang, L. C. Disordered Atomic Packing Structure of Metallic Glass: Toward Ultrafast Hydroxyl Radicals Production Rate and Strong Electron Transfer Ability in Catalytic Performance. *Adv. Funct. Mater.* **2017**, *27*, 1702258.

(28) Liang, S. X.; Jia, Z.; Liu, Y. J.; Zhang, W.; Wang, W.; Lu, J.; Zhang, L. C. Compelling Rejuvenated Catalytic Performance in Metallic Glasses. *Adv. Mater.* **2018**, *30*, 1802764.

(29) Jia, Z.; Wang, Q.; Sun, L.; Wang, Q.; Zhang, L. C.; Wu, G.; Luan, J. H.; Jiao, Z. B.; Wang, A.; Liang, S. X.; Gu, M.; Lu, J. Attractive In Situ Self-Reconstructed Hierarchical Gradient Structure of Metallic Glass for High Efficiency and Remarkable Stability in Catalytic Performance. *Adv. Funct. Mater.* **2019**, *29*, 1807857.

(30) Yu, J.; Ding, Y.; Xu, C.; Inoue, A.; Sakurai, T.; Chen, M. Nanoporous Metals by Dealloying Multicomponent Metallic Glasses. *Chem. Mater.* **2008**, *20*, 4548−4550.
(31) Yang, X.; Xu, W.; Cao, S.; Zhu, S.; Liang, Y.; Cui, Z.; Yang, X.; Li, Z.; Wu, S.; Inoue, A.; Chen, L. An amorphous nanoporous PdCuNi-S hybrid electrocatalyst for highly efficient hydrogen production. *Appl. Catal., B* **2019**, *246*, 156−165.
(32) Xu, Y.; Cheng, J.; Yiu, P. M.; Shan, G.; Shibayama, T.; Watanabe, S.; Ohnuma, M.; Shek, C.-H. Evolution of 3D nanoporosity and morphology in selectively dealloying ternary Au55Cu25Si20 metallic glass ribbon with enhanced alcohol electro-oxidation performance. *Nanoscale* **2018**, *10*, 18846−18856.
(33) Jia, Z.; Jiang, J.-L.; Sun, L.; Zhang, L.-C.; Wang, Q.; Liang, S.-X.; Qin, P.; Li, D.-F.; Lu, J.; Kruzic, J. J. Role of Boron in Enhancing Electron Delocalization to Improve Catalytic Activity of Fe-Based Metallic Glasses for Persulfate-Based Advanced Oxidation. *ACS Appl. Mater. Interfaces* **2020**, *12*, 44789−44797.
(34) Jia, Z.; Nomoto, K.; Wang, Q.; Kong, C.; Sun, L.; Zhang, L. C.; Liang, S. X.; Lu, J.; Kruzic, J. J. A Self-Supported High-Entropy Metallic Glass with a Nanosponge Architecture for Efficient Hydrogen Evolution under Alkaline and Acidic Conditions. *Adv. Funct. Mater.* **2021**, *31*, 2101586.
(35) Jia, Z.; Yang, T.; Sun, L.; Zhao, Y.; Li, W.; Luan, J.; Lyu, F.; Zhang, L.-C.; Kruzic, J. J.; Kai, J.-J.; Huang, J. C.; Lu, J.; Liu, C. T. A Novel Multinary Intermetallic as an Active Electrocatalyst for Hydrogen Evolution. *Adv. Mater.* **2020**, *32*, 2000385.
(36) Grimme, S. Semiempirical GGA-type density functional constructed with a long-range dispersion correction. *J. Comput. Chem.* **2006**, *27*, 1787−1799.
(37) Nørskov, J. K.; Bligaard, T.; Logadottir, A.; Kitchin, J. R.; Chen, J. G.; Pandelov, S.; Norskov, J. K. Trends in the exchange current for hydrogen evolution. *J. Electrochem. Soc.* **2005**, *152*, J23−J26.
(38) Yu, F.; Zhou, H.; Huang, Y.; Sun, J.; Qin, F.; Bao, J.; Goddard, W. A.; Chen, S.; Ren, Z. High-performance bifunctional porous non-noble metal phosphide catalyst for overall water splitting. *Nat. Commun.* **2018**, *9*, 2551.
(39) Qi, Z.; Lee, W. XPS study of CMP mechanisms of NiP coating for hard disk drive substrates. *Tribol. Int.* **2010**, *43*, 810−814.
(40) Hu, F.; Zhu, S.; Chen, S.; Li, Y.; Ma, L.; Wu, T.; Zhang, Y.; Wang, C.; Liu, C.; Yang, X.; Song, L.; Yang, X.; Xiong, Y. Amorphous Metallic NiFeP: A Conductive Bulk Material Achieving High Activity for Oxygen Evolution Reaction in Both Alkaline and Acidic Media. *Adv. Mater.* **2017**, *29*, 1606570.
(41) Yu, L.; Zhu, Q.; Song, S.; McElhenny, B.; Wang, D.; Wu, C.; Qin, Z.; Bao, J.; Yu, Y.; Chen, S.; Ren, Z. Non-noble metal-nitride based electrocatalysts for high-performance alkaline seawater electrolysis. *Nat. Commun.* **2019**, *10*, 5106.
(42) Yang, Y.; Zhang, K.; Lin, H.; Li, X.; Chan, H. C.; Yang, L.; Gao, Q. MoS2−Ni3S2 Heteronanorods as Efficient and Stable Bifunctional Electrocatalysts for Overall Water Splitting. *ACS Catal.* **2017**, *7*, 2357−2366.
(43) Jia, X.; Zhao, Y.; Chen, G.; Shang, L.; Shi, R.; Kang, X.; Waterhouse, G. I. N.; Wu, L.-Z.; Tung, C.-H.; Zhang, T. Ni3FeN Nanoparticles Derived from Ultrathin NiFe-Layered Double Hydroxide Nanosheets: An Efficient Overall Water Splitting Electrocatalyst. *Adv. Energy Mater.* **2016**, *6*, 1502585.
(44) Liu, H.; Zou, J.; Ding, Y.; Liu, B.; Wang, Y. Novel α-FeOOH corner-truncated tetragonal prisms: crystal structure, growth mechanism and lithium storage properties. *J. Appl. Electrochem.* **2019**, *49*, 657−669.
(45) Xiao, L.; Su, T.; Wang, Z.; Zhang, K.; Peng, X.; Han, Y.; Li, Q.; Wang, X. Enhanced Photocatalytic Hydrogen Evolution by Loading Cd0.5Zn0.5S QDs onto Ni2P Porous Nanosheets. *Nanoscale Res. Lett.* **2018**, *13*, 31.
(46) Jiang, J. L.; Jia, Z.; He, Q.; Wang, Q.; Lyu, F.; Zhang, L. C.; Liang, S. X.; Kruzic, J. J.; Lu, J. Synergistic function of iron and cobalt in metallic glasses for highly improving persulfate activation in water treatment. *J. Alloys Compd.* **2020**, *822*, 153574.
(47) Jiao, Y.; Zheng, Y.; Jaroniec, M.; Qiao, S. Z. Design of electrocatalysts for oxygen- and hydrogen-involving energy conversion reactions. *Chem. Soc. Rev.* **2015**, *44*, 2060−2086.
(48) Ye, S.-H.; Shi, Z.-X.; Feng, J.-X.; Tong, Y.-X.; Li, G.-R. Activating CoOOH Porous Nanosheet Arrays by Partial Iron Substitution for Efficient Oxygen Evolution Reaction. *Angew. Chem., Int. Ed.* **2018**, *57*, 2672−2676.
(49) Chemelewski, W. D.; Lee, H.-C.; Lin, J.-F.; Bard, A. J.; Mullins, C. B. Amorphous FeOOH Oxygen Evolution Reaction Catalyst for Photoelectrochemical Water Splitting. *J. Am. Chem. Soc.* **2014**, *136*, 2843−2850.
(50) Greeley, J.; Jaramillo, T. F.; Bonde, J.; Chorkendorff, I.; Nørskov, J. K. Computational high-throughput screening of electrocatalytic materials for hydrogen evolution. *Nat. Mater.* **2006**, *5*, 909−913.

https://doi.org/10.1021/acsami.1c22294
ACS Appl. Mater. Interfaces 2022, 14, 10288−10297